Numerical and experimental evaluation of nasopharyngeal aerosol administration methods in children with adenoid hypertrophy

International Journal of Pharmaceutics 653 (2024) 123906

Contents lists available at ScienceDirect

International Journal of Pharmaceutics

journal homepage: www.elsevier.com/locate/ijpharm

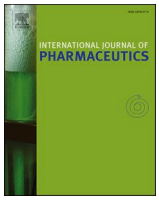

Numerical and experimental evaluation of nasopharyngeal aerosol administration methods in children with adenoid hypertrophy

Zhenzhen Hu [a,b,f], Shaokoon Cheng [c], Siping Sun [d], Yusheng Wang [a], Miao Lou [e], Ruiping Ma [a], Minjie Gong [a], Feilun Yang [a], Guoxi Zheng [a], Ya Zhang [a,*], Jingliang Dong [a,f,g,*]

[a] Department of Otolaryngology Head and Neck Surgery, The Second Affiliated Hospital of Xi'an Jiaotong University, Xi'an, Shaanxi 710004, China
[b] School of Engineering, RMIT University, Bundoora, VIC 3083, Australia
[c] School of Engineering, Faculty of Science and Engineering, Macquarie University, Sydney, NSW 2109, Australia
[d] Zhejiang Cuize Pharmtech Co. Ltd., Hangzhou, Zhejiang 310000, China
[e] Department of Otorhinolaryngology Head and Neck Surgery, Shaanxi Provincial People's Hospital, Xi'an, Shaanxi 710068, China
[f] Institute for Sustainable Industries & Liveable Cities, Victoria University, PO Box 14428, Melbourne, VIC 8001, Australia
[g] First Year College, Victoria University, Footscray Park Campus, Footscray, VIC 3011, Australia

ARTICLE INFO

Keywords:
Adenoid hypertrophy
Intranasal administration
Aerosol delivery
Nasopharynx targeting
Particle deposition

ABSTRACT

Administering aerosol drugs through the nasal pathway is a common early treatment for children with adenoid hypertrophy (AH). To enhance therapeutic efficacy, a deeper understanding of nasal drug delivery in the nasopharynx is essential. This study uses an integrated experimental, numerical modelling approach to investigate the delivery process of both the aerosol mask delivery system (MDS) and the bi-directional delivery system (BDS) in the pediatric nasal airway with AH. The combined effect of respiratory flow rates and particle size on delivery efficiency was systematically analyzed. The results showed that the nasopharyngeal peak deposition efficiency (DE) for BDS was approximately 2.25–3.73 times higher than that for MDS under low-flow, resting and high-flow respiratory conditions. Overall nasopharyngeal DEs for MDS were at a low level of below 16 %. For each respiratory flow rate, the BDS tended to achieve higher peak DEs (36.36 % vs 9.74 %, 37.80 % vs 14.01 %, 34.58 % vs 15.35 %) at smaller particle sizes (15 μm vs 17 μm, 10 μm vs 14 μm, 6 μm vs 9 μm). An optimal particle size exists for each respiratory flow rate, maximizing the drug delivery efficiency to the nasopharynx. The BDS is more effective in delivering drug aerosols to the nasal cavity and nasopharynx, which is crucial for early intervention in children with AH.

1. Introduction

Adenoids (nasopharyngeal tonsils) are masses of lymphoid tissue located at the junction of the roof and the posterior wall of the nasopharynx, constituting a part of Waldeyer's ring (Niedzielski et al., 2023). Research has shown that the etiology of adenoid hypertrophy (AH) is associated with abnormal immune responses, infections, environmental exposure, and hormonal or genetic factors (Niedzielski et al., 2023; Ahmad et al., 2023). Common clinical symptoms include runny nose, nasal congestion, snoring, mouth breathing, sleep apnea, speech disorders, and developmental delays. Some affected children may also exhibit adenoid facies, characterized by a narrow or "V"-shaped maxillary arch, a retropositioned hyoid bone, and a retrocontractioned mandible (Koca et al., 2016; Pawlowska-Seredynska et al., 2020). Timely detection and early treatment are crucial for AH, which can help prevent further complications. Intranasal corticosteroid therapy has consistently been the most common treatment method for AH and its associated symptoms (Zwierz et al., 2023). However, the effectiveness of nasal aerosol therapy largely depends on how much medication can reach the infected nasal mucosal surfaces. Therefore, improving the delivery performance of drug aerosols to ensure precise targeting of the nasopharynx is crucial for the treatment efficacy of AH.

Commonly used delivery devices today are nasal spray pumps, aerosol mask delivery systems (MDS), and breath-powered bi-directional delivery systems (BDS). Spray pumps are traditionally widely used in nasal administration due to their ease of operation. However, the high ejection speed and relatively large particle size associated with spray pumps typically lead to the deposition of most particles in the

* Corresponding authors.
E-mail addresses: zhangya@xjtu.edu.cn (Y. Zhang), jingliang.dong@vu.edu.au (J. Dong).

https://doi.org/10.1016/j.ijpharm.2024.123906
Received 13 November 2023; Received in revised form 3 February 2024; Accepted 13 February 2024
Available online 15 February 2024

anterior nasal cavity, with only a small fraction of the particles penetratinge through the nasal valve (Bateman et al., 2002; Kimbell et al., 2007; Inthavong et al., 2011), ultimately leading to poor treatment efficacy for AH. An additional challenge associated with the use of spray pumps is the positioning of the nasal spray bottle. The direction and depth of insertion of the nasal spray bottle nozzle can significantly impact the delivery efficiency to the target area, as indicated by Tong et al. (2016), thereby increases the uncertainty of therapeutic efficacy. In this study, our primary research focus is on evaluating the aerosol delivery performance using MDS and BDS approaches. Compared to spray pumps, nebulizer inhalation therapy can provide the concurrent administration of multiple drug types and offers user comfort as individuals only need to exhibit tidal breathing when using the devices. Lin et al. (2012) studied in vitro the effect of nebulizer type, actuation mechanisms and different aerosol masks on lung deposition performance in spontaneously breathing children and showed that aerosol mask design can affect inhaled drug dose across the tested nebulizers. Subsequently, Lin et al. (2015) investigated the impact of two aerosol masks connected to the vibrating mesh nebulizer on aerosol delivery performance in a pediatric lung model at different flow rates under a high-flow humidity system. They demonstrated that the flow of gas entering the mask and breathing patterns affect aerosol delivery, independent of the mask used. Recently, Chiang et al. (2023) assessed the impact of three face masks designed for a jet nebulizer, including an aerosol mask, a modified non-rebreathing mask (without vent holes), and an AerosoLess mask, on fugitive aerosol concentration during nebulization using a lung simulator. The results indicated that a filtered mask had an advantage in reducing the concentration of fugitive aerosols in the environment. Hosseini et al. (2019) compared the efficacy of nasal sprays and Mucosal Atomization Device (MAD) atomizer in terms of regional delivery in nasal airway replica of 2-, 5- and 50-year-old subjects. The results showed that nasal sprays are not suitable for pediatric populations because of narrower nasal passages and greater anterior deposition (~60 %); whereas MAD atomizer resulted in significantly less anterior deposition (~10 %-15 %).

In recent years, a novel breath-powered bi-directional drug delivery concept has been proposed, which takes advantage of the posterior connection between the two nasal passages persisting when the soft palate automatically closes during oral exhalation. The exhalation airflow carrying the aerosol enters one side of the nasal cavity through a sealed nosepiece and exits the other. Compared to traditional nasal inhalation nebulizers, bi-directional delivery technology significantly minimizes the risks and issues associated with lung deposition (Djupesland et al., 2004). Farnoud et al. (Farnoud et al., 2020; Farnoud et al., 2021) investigated the impact of nosepiece tilt angles (45° and 90°) on intranasal aerosol dispersion and deposition during bi-directional pulsatile flow administration and compared it with bi-directional administration with non-pulsatile flow. The study revealed that nosepiece with clockwise inclination of 45° was more advantageous for drug-aerosol delivery, and pulsatile flow minimized the deposition imbalance between the left and right nasal chambers. Xi et al. (Xi et al., 2017; Xi et al., 2018) quantitatively compared drug deposition in the nasal cavity and olfactory region under normal and bi-directional breathing modes and analyzed the impact of nasal dilation on deposition. The results indicated that bi-directional delivery resulted in higher deposition in both the nasal cavity and olfactory region, while nasal dilation led to a reduction in the total nasal deposition for both delivery methods but an increased dose in the olfactory region. Hosseini and Golshahi (2019) evaluated nasal and paranasal drug delivery with nebulizers, with and without pulsating airflow, in nasal airway replicas of 2-, 5- and 50-year-old human subjects, considering normal and bi-directional breathing techniques. The results showed that paranasal delivery was significantly enhanced using pulsating nebulization under bi-directional breathing administration technique for all subjects and airway morphology resulted in significantly different drug delivery efficiency. Dong et al. (2017) compared the delivery efficiency of mask administration and bi-directional administration in the olfactory region of a 60-year-old healthy male and reported that the bi-directional delivery method could promote olfactory region deposition. While extensive research has been conducted, previous studies have primarily focused on adult subjects and often involved one case, with very limited studies of nasal deposition in children. Due to the unique anatomical structure of the pediatric nasal cavity, which is not merely a scaled-down version of the adult nasal cavity, previous research findings are unlikely applicable to children.

Wilkins et al. (2021) used the MAD Nasal™ device to perform local intranasal vaccine delivery in nasal replicas of five subjects aged 3–24 months and measured their delivery efficiency. The results showed no significant differences in total delivery efficiency between the five models; however, regional deposition patterns differed. Subsequently, Li et al. (2023) investigated the correlation between spray characteristics and local deposition efficiency of four intranasal delivery devices in nasal airway replicas of infants aged 3–24 months. They reported that all four devices performed consistently in terms of spray characteristics and were able to deliver more than 80 % of the candidate vaccine to the target area. In addition, the delivery efficiency was affected by either the spray droplet size distribution or the distance between the nozzle tip and the internal nasal valve. It is evident that these studies have focused mainly on the nasal cavity of healthy infants, with significantly fewer studies on the nasal cavity of children suffering from pathological changes. Two of our previous studies numerically simulated the deposition of Artemisia pollen and 1–20 μm particles, respectively, in the nasal airways of children with AH (Hu et al., 2023b; Sun et al., 2023), focusing on the deposition behaviour of the particles under voluntary respiration. In order to more effectively alleviate clinical symptoms in children with AH, it is necessary to understand the delivery effects of commonly used drug administration devices in the nasopharynx.

This study aims to understand the factors influencing aerosol deposition in the nasopharynx of children with AH and further enhance the delivery efficiency to the nasopharynx. To this end, we compared the drug aerosol delivery performance between the breath-powered BDS and the aerosol MDS in five anatomically accurate nasal airway models of children with AH reconstructed from CT scans, and systematically elucidated the integrated impact of respiratory flow rate and particle size on delivery efficiency. This study results can provide scientific guidance for intranasal administration in children with AH, ultimately facilitating improvements in clinical treatment outcomes.

2. Materials and methods

2.1. Three-dimensional models and aerosol delivery systems

Anatomically accurate three-dimensional models of the pediatric airway were reconstructed from computed tomography (CT) scan images in the Digital Imaging and Communications in Medicine (DICOM) format. The CT image pixel size was 0.39 × 0.39 mm, the image dimensions were 512 × 512, and the slice thickness was 0.5 mm. CT images in DICOM format were imported into the Mimics software (Materialise, Belgium) to reconstruct the nasal airway (including the nasal cavity, nasopharynx, and maxillary sinuses). Further details on model reconstruction and validation can be found in previous works (Hu et al., 2023a; Hu et al., 2023b; Dong et al., 2016). A total of 5 pediatric models were constructed, consisting of four males and one female, with an average age of 5 ± 1.58 years (Fig. 1). Important model information on the five subjects has been included in Table 1. The size of adenoids and the patency of the nasopharyngeal airway can be reflected by the adenoidal nasopharyngeal (AN) ratio (Fujioka et al., 1979). An AN ratio above 0.6 is an indication of AH (Elwany, 1987). In this study, the AN ratios for the five children were 0.89 (Subject A), 0.86 (Subject B), 0.81 (Subject C), 0.76 (Subject D) and 0.77 (Subject E), with an average AN ratio of 0.818 ± 0.056. Detailed method for AN ratio measurement can be referred to our previous work (Hu et al., 2023a; Hu et al., 2023b).

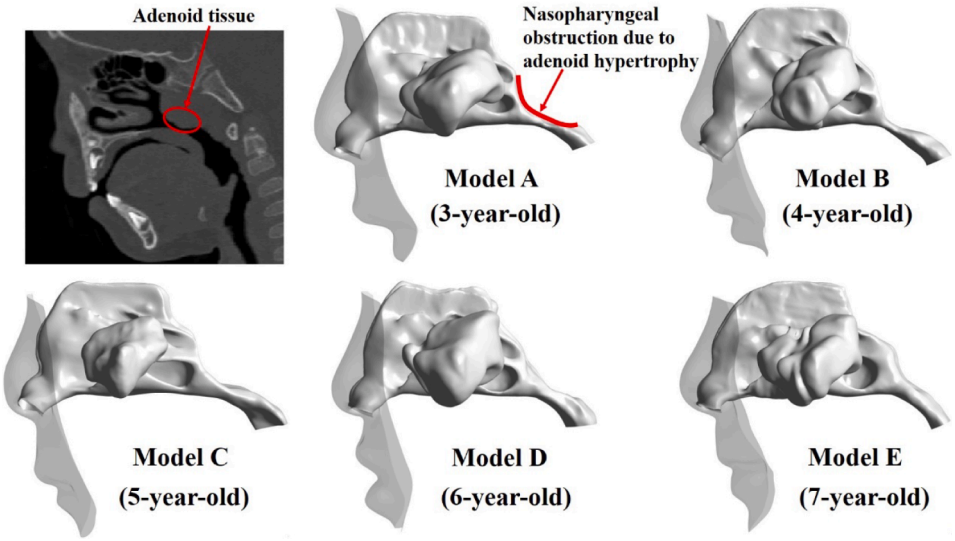

Fig. 1. Three-dimensional children nasal airway models with adenoid hypertrophy.

Table 1
Key model information about the subject.

Subject	Age	Sex	Nasopharyngeal surface area (cm^2)	Nasopharyngeal volume (cm^3)	AN ratio
Subject A	3-year-old	Male	9.55	1.47	0.89
Subject B	4-year-old	Male	9.92	1.64	0.86
Subject C	5-year-old	Male	11.31	1.89	0.81
Subject D	6-year-old	Female	10.96	2.35	0.76
Subject E	7-year-old	Male	10.48	2.29	0.77

According to the AN ratio, Adedeji et al. (2016) classified the degree of nasopharyngeal airway obstruction by adenoids as mild (0.60 ~ 0.69), moderate (0.70 ~ 0.79) and severe (0.80 ~ 0.89). The five children in this study were categorised as having moderate AH for Subject D (0.76) and Subject E (0.77); severe AH for Subject A (0.89), Subject B (0.86), and Subject C (0.81) based on the AN ratio. This study obtained approval from the Institutional Review Board of the Second Affiliated Hospital of Xi'an Jiaotong University (Approval No. 2021–186) and obtained informed consent from the parents of the pediatric patients.

We selected the standard aerosol mask connected to the nebulizer and the breath-powered bi-directional device for data analysis and performance comparison. The principle of the MDS is illustrated in Fig. 2A. Aerosol medication is nebulized into the mask at a controlled concentration, and both nasal chambers simultaneously inhale aerosol particles that pass through the choana into the nasopharynx, with some particles escaping into the lower respiratory tract. The principle of the BDS is illustrated in Fig. 2B. The intraoral pressure generated during oral exhalation elevates the soft palate, thereby closing off the nasopharynx; consequently, our three-dimensional model extends only up to the

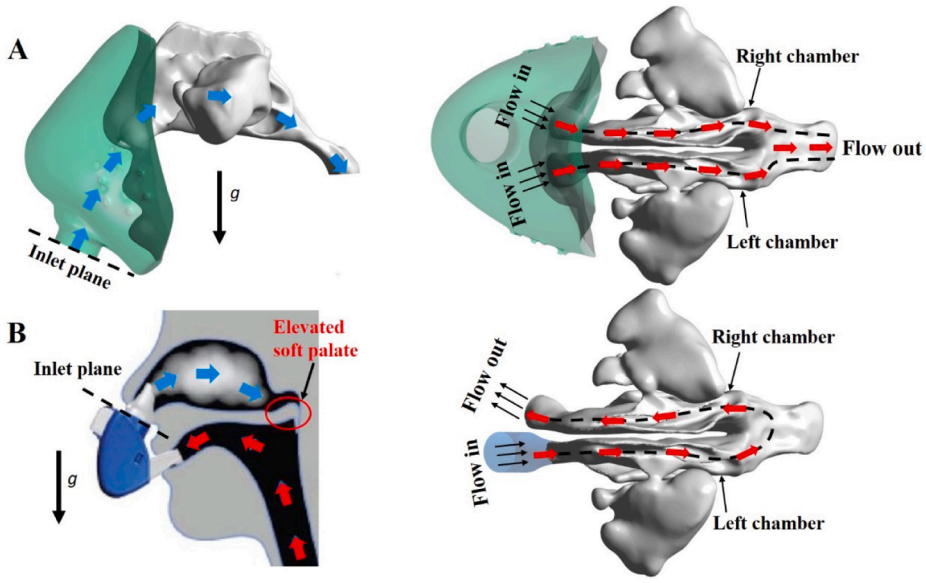

Fig. 2. Schematic representation of aerosol mask (A) and bi-directional (B) delivery methods.

nasopharynx to simulate the closure of the soft palate during BDS delivery. It is imperative that the nosepiece of the drug delivery device is inserted tightly into one nostril (left nostril in this study) during operation to ensure that there is no air leakage between the nosepiece and the anterior nostril interface. Exhaled airflow carrying aerosol particles first enters the left chamber (LC), then passes through the choana into the nasopharynx, and finally exits through the anterior nostril of the right chamber (RC) into the surrounding environment. During exhalation, the elevation of the soft palate seals off the nasopharynx, preventing small particles from entering the lower respiratory tract. The black dashed line and the red thick arrows represent the aerosol flow path and direction of the two methods, respectively.

Based on anatomical structure and functional considerations, the delivery device and pediatric model were divided into 11 regions (Fig. 3), with the nasopharynx as the target for drug delivery in this study. In this study, the average surface area of the nasopharynx in the five children with AH was 10.44 ± 0.72 cm^2, and the average volume was 1.93 ± 0.39 cm^3.

2.2. Mesh generation and boundary conditions

ANSYS Fluent Meshing (Ansys Inc., Canonsburg, Pennsylvania) was used to generate polyhedral meshes. The mesh size in the nosepiece region ranged from 0.05 to 0.1 mm, expected to be sufficient for the dense spray to fluid momentum exchange. Five layers of prism mesh were attached to the nasal wall, with the first layer having a height of 0.02 mm and a growth rate of 1.1 (Fig. 4). The final mesh number of each model was approximately 2.3 to 2.5 million elements, equivalent to approximately 8.05 to 8.75 million tetrahedral elements. Previous works (Hu et al., 2023a; Hu et al., 2023b) from the authors have demonstrated that the above mesh quality ascertained a balance between computational efficiency and accuracy.

The tidal volume and respiratory rate for children aged 3–7 years were obtained from data reported by Hofmann (1982), and the duration of the respiratory cycle was obtained from data reported by Thiriet (2014). The resting respiratory flow rates for children aged 3–7 years were 7.84, 9.03, 9.77, 10.72, and 11.47 L/min, respectively. Table 2 presents the respiratory parameters under quiet breathing conditions based on the literature. Under low-flow respiratory conditions (half the resting flow rate), the respiratory flow rates were set at 3.92, 4.52, 4.89, 5.36, and 5.74 L/min, respectively. Under high-flow respiratory conditions (double the resting flow rate), the respiratory flow rates were set at 15.68, 18.06, 19.54, 21.44, and 22.94 L/min, respectively.

For the MDS, the inlet of the mask was set as a "pressure inlet" with a gauge pressure of zero, assuming that the mask was exposed to the atmosphere. The outlet of the nasopharynx was set as a "velocity outlet," with velocity magnitude calculated by dividing the volumetric flow rate by the outlet area. For the BDS, the outlet of the nasopharynx was closed and treated as a wall. The "velocity inlet" was set at the annular region around the nosepiece tip. The cross-sectional profile of this region is circular with an area of 8.49×10^{-5} m^2. The inlet velocity was calculated using the exhalation flow rate and the cross-sectional area. The spray is introduced into the nasal cavity from the nosepiece tip located inside the nostril. The outlet of the other nostril was set as a "pressure outlet" with a gauge pressure of zero. The boundary conditions for particle–wall interactions were set to "trap". A no-slip, stationary boundary condition was applied to the nasal walls. The respiratory airflow is considered as steady and incompressible.

2.3. Airflow simulation and particle tracking

The k-ω SST model was chosen to simulate the characteristics of airflow dynamics in the nasal airways of children with AH. The momentum and turbulence equations were discretized using the First Order Upwind format, and the SIMPLE method was used for pressure–velocity coupling.

The Lagrangian Discrete Phase Model (DPM) was utilized to predict the transport and deposition characteristics of particles within the nasal airway, considering gravity, drag force, and Brownian forces (Inthavong et al., 2016; Inthavong et al., 2009). For the low volume fraction dispersed phase (drug particles in this study), a one-way coupled Lagrangian approach was employed,

$$\frac{du_i^p}{dt} = F_D + F_G + F_B\# \tag{1}$$

where u_i^p is the particle velocity, F_D is the drag force per unit particle mass described as:

$$F_D = \frac{18\mu(u_i^g - u_i^p)}{C_c d_p^2 \rho_p}\# \tag{2}$$

where u_i^g is the airflow velocity, μ is the air viscosity, d_p is the particle diameter, ρ_p is the particle density, and C_c is the Cunningham correction factor given by:

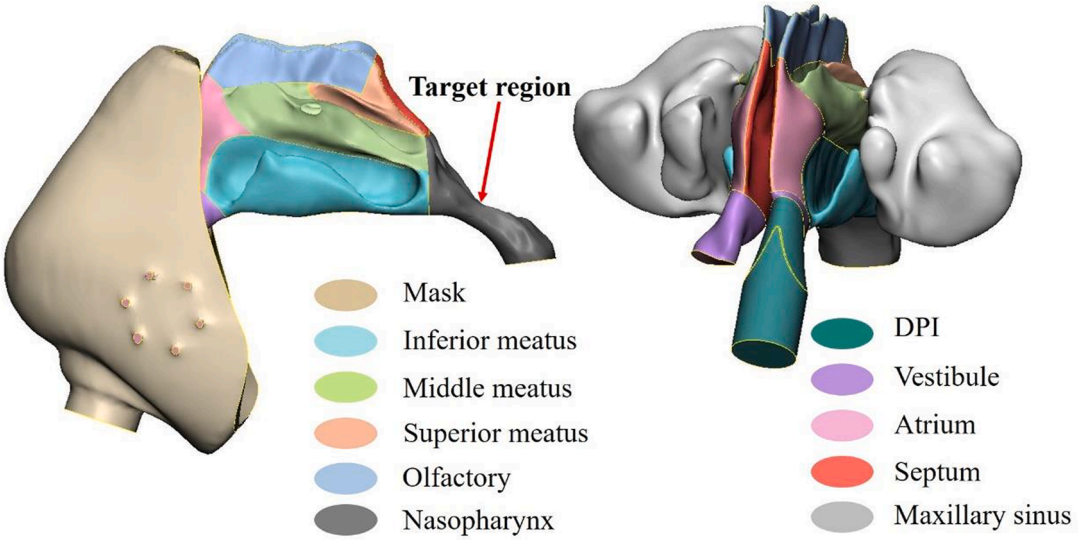

Fig. 3. Surface partitioning of delivery systems: Left – aerosol mask system (MDS), Right – bi-directional delivery system (BDS).

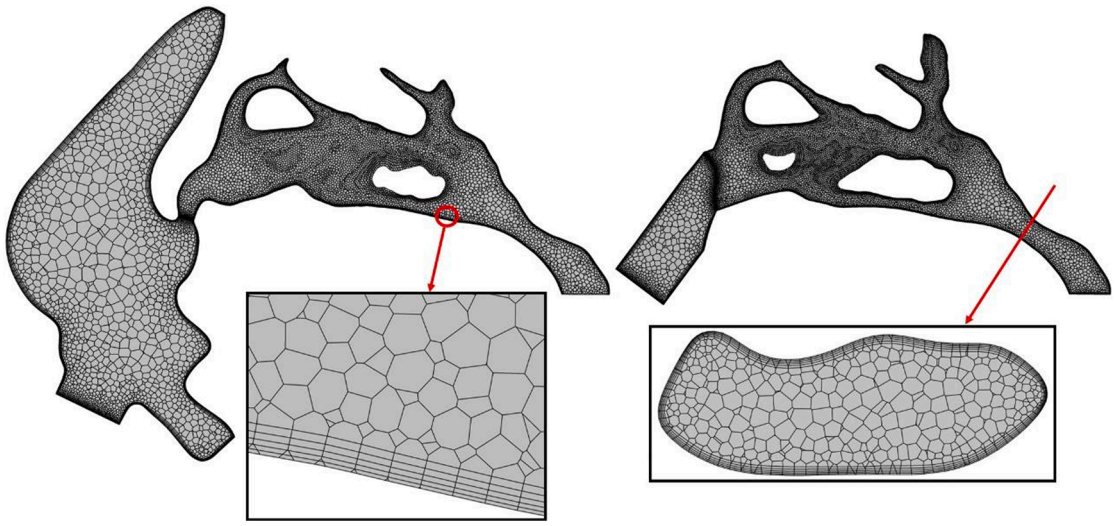

Fig. 4. Mesh preview results: Left – internal polyhedral mesh, Right – near wall prism mesh.

Table 2
Respiratory parameters under quiet breathing conditions.

Subject	Tidal volume (mL)	Respiratory rate (breaths/min)	Minute ventilation (mL/min)	Inspiration-to-expiration time ratio	Inhalation flow rate (L/min)
3-Year-Old	121	24	2904	1:1.7	7.84
4-Year-Old	152	22	3344	1:1.7	9.03
5-Year-Old	181	20	3620	1:1.7	9.77
6-Year-Old	209	19	3971	1:1.7	10.72
7-Year-Old	236	18	4248	1:1.7	11.47

The parameters were obtained from the reference (Hofmann,1982; Thiriet, 2014).

$$C_c = 1 + \frac{2\lambda}{d_p}\left(1.257 + 0.4e^{-\frac{1.1d_p}{2\lambda}}\right)\# \tag{3}$$

where λ is the air molecular mean free path, assumed to be 67 nm.

Brownian force (F_B) is of the form $\xi_i\sqrt{(\pi S_o)/\Delta t}$, where ξ_i are zero-mean, unit-variance-independent Gaussian random numbers, and Δt is the particle integration time-step. S_o is a spectral intensity function:

$$S_o = \frac{216\nu k_B T}{\pi^2 \rho d_p^5 \left(\frac{\rho_p}{\rho}\right)^2 C_c}\# \tag{4}$$

The aerosol particles were assumed to be spherical with a unit density (ρ_p) of 1000 kg/m^3, while the air density (ρ) was 1.225 kg/m^3. ν is the kinematic viscosity, T is the Kelvin temperature of inhaled air (293 K), k_B is the Boltzmann constant, and C_c is the Cunningham correction factor.

The target region of this study is the nasopharynx in children with AH. If the diameter of the aerosol particles was too large, the particles were mainly deposited in the anterior part of the nasal cavity due to inertia, which had minimal impact on the nasopharynx. In addition, previous studies have shown that typical aerosol sizes produced by commonly used nebulizers, metered-dose inhalers, and dry-powder inhalers are generally below 20 μm (Groneberg et al., 2003; Wang et al., 2017). Hence, we chose particles ranging from 1 to 20 μm for the subsequent numerical simulation and deposition analysis of this study, aiming to explore deposition patterns and determine optimal particle sizes for delivery drug aerosols specifically to the nasopharyngeal region. For each particle size, 50,000 particles were released from the inlet plane of the device. Deposition efficiency (DE) = the mass of drug deposited in a specific region / the total mass of drug released from the device × 100 %. In this study, DE is presented as mean ± standard deviation. The deposition of inhaled particles in the nasal cavity depends on the geometric shape of the nasal cavity, respiratory flow rate, and particle properties such as size, shape, and density (Kesavan et al., 2000; Cheng, 2003). It is acknowledged that the drug delivery process is influenced by multiple factors simultaneously. However, in order to narrow the research scope to a manageable level, the present study has chosen to focus on examining the impact of aerosol particle size and respiratory flow rate on drug delivery efficiency.

2.4. Model validation methods

Two approaches were used to validate aerosol particle deposition to ascertain the fidelity of the models. The first validation approach is achieved by comparing the results with depositional data from the literature. The impact parameter ($d2\ aeQ$) is widely used to determine the particle DE, which takes into account both particle size and flow rate, where d_{ae} is the aerodynamic equivalent diameter (μm) and Q is the volumetric flow rate (L/min). We compared the deposition results for flow rates ranging from 7.8 to 11.5 L/min and particle diameters ranging from 1 to 30 μm with published data for children.

The second validation was performed using in-vitro deposition experiments. Physical replicas of the children's nasal airways were fabricated using a stereolithography (STL) 3D printer. The 3D-printed model was sectioned into seven parts to allow for disassembly (Fig. 5). The outer nose (Fig. 5) was created as a separate component using liquid silicone rubber, which provides a tight interference fit with the device to prevent air leakage. The irregular nasopharyngeal outlet was designed as a cylinder (Fig. 5) to enable connection to a low-volume pump (LCP 5, COPLEY, UK). To seal each part of the model together, we affixed sealing strips and used screws to connect each pore (Fig. 5).

The experimental platform for the MDS is shown in Fig. 6A. Each component of the model and the outer nose were assembled and fixed on the model stand before the experiment. The mask connected to the nebulizer (PHILIPS, China) was secured around the outer nose and the nasopharyngeal outlet of the model was connected to a low volume pump (LCP 5, COPLEY, UK) to simulate respiratory airflow. The experimental platform for the BDS is shown in Fig. 6B. The nasopharyngeal outlet of the model was sealed with Blu-Tack to simulate closure during BDS administration. The nosepiece of the bi-directional drug

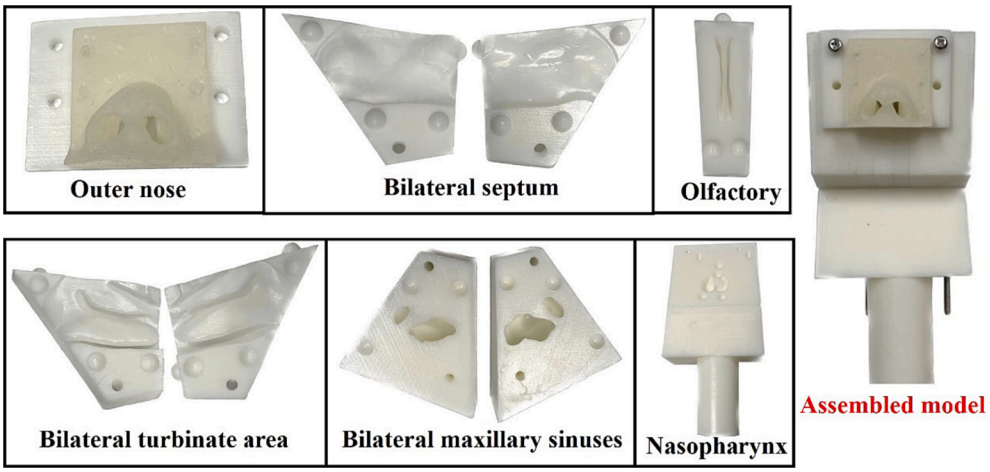

Fig. 5. 3D printed bionic model that consists silicone outer nose and internal major components of the nasal airway.

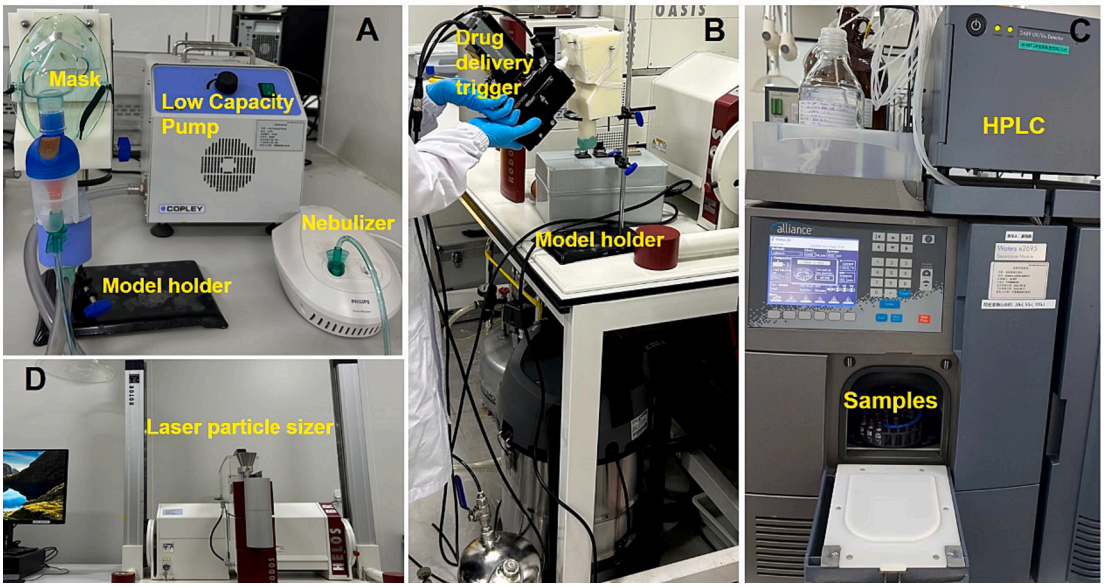

Fig. 6. In vitro experimental rig for measuring the drug aerosol delivery performance of both approaches: the mask delivery system (A), the bi-directional delivery system (B), High-Performance Liquid Chromatograph (C), and Laser Particle Sizer (D).

delivery device was inserted into one nostril of the model, and care was taken to ensure no air leakage. The drug delivery device was connected to the trigger (DH-ROBOTICS, China) to simulate drug delivery. The model was disassembled after each experiment, and the drug deposited in each region was eluted. The deposited dose in each region was then quantified using the high-performance liquid chromatograph (HPLC, Waters e2695, WATERS, USA). The in vitro deposition experiments were performed in a 3D printed nasal airway replica of Subject D. Budesonide (AstraZeneca Pty Ltd., 2 ml:1 mg) was used for the mask drug delivery trial and mometasone furoate (Merck & Co., lnc., 0.05 %) was used for the bi-directional drug delivery trial, both of which are commercially available and commonly used drugs. Particle size distributions of mask nebulised budesonide and bi-directionally administered mometasone furoate nasal sprays were measured by laser particle sizer (HELOS IA-019, SYMPATEC, Germany). The measurement principle is to use the diffraction phenomenon of light, i.e. large particles produce small diffraction angles and small particles produce large diffraction angles, to give the particle size and size distribution of the particles by calculating the light intensity distribution of the different diffraction figures collected on the detector. Subsequently, numerical simulations were carried out under resting and high-flow respiratory conditions, respectively.

2.5. Quantification of regional deposition

The nasal airway model was carefully disassembled after each deposition experiment. To ensure that all drugs on each module were washed off, we eluted budesonide from the surface of each module into a 50 ml volumetric flask using diluent (acetonitrile: phosphate buffer = 35:65 (v/v)). For mometasone furoate, the same thorough elution was performed with diluent (glacial acetic acid: acetonitrile: water = 5:1000:1000 (v/v/v)). The volumetric flask was then sonicated for 5 min to better dissolve the eluted down sample. Prior to HPLC analysis, samples and standards were filtered through syringe filters (PTFE membrane, 0.45 μm pore size, 02036331-TYLQ-0014, Titan). Finally, HPLC was used to quantify the regional deposition of nasal airway replicas. Table 3 provides all HPLC settings for the analytical quantification of budesonide and mometasone furoate.

To calculate the total delivered dose for the in vitro deposition test, the drug administration device was weighed before and after each test

Table 3
Summary of methods used for High Performance Liquid Chromatography (HPLC).

Models	Budesonide (MDS)	Mometasone Furoate (BDS)
Mobile phase	Anhydrous ethanol: acetonitrile: phosphate buffer = 2:35:65 (v/v/v)	Acetonitrile: water = 47:53 (v/v)
Injection Volume	50 μl	20 μl
UV detection	240 nm	254 nm
Column	120 EC-C18 4.6 × 100 mm, 2.7 μm	C18 4.6 × 75 mm, 2.7 μm
Column temperature	50 °C	40 °C
Flow rate	1.0 ml/min	2.0 ml/min
Retention time	8.5 min, 9.5 min	3.6 min

using an analytical laboratory balance (XSE205DU, METTLER TOLEDO) with an accuracy of 0.01 mg. Drug recovery efficiency = total dose recovered in the whole nasal model / total delivered dose × 100 %. Regional delivery efficiency = recovered dose in the region of interest / total recovered dose × 100 %.

3. Results and discussion

3.1. Model validation

As illustrated in Fig. 7, deposition data obtained from this work are in good agreement with the in vivo deposition data of Becquemin et al. (1991) and Bennett et al. (2008). While the DE within the nasal replicas of Golshahi et al. (2011) and Zhou et al. (2013) is slightly higher than ours. This deposition discrepancy is mainly due to the fact that our model does not retain the larynx, thus resulting in a relatively low DE. In addition, the inhalation flow rate of our model is relatively low, which also results in a lower number of particles deposited by direct impaction.

With our experimental method, the recoveries of the tested samples were all above 90 %, indicating that the method can accurately elute down the samples. The median particle size (D50) of budesonide was 7.61 μm and that of mometasone furoate was 39.5 μm as measured by laser particle sizer. The deposition results of the in vitro experiments for MDS and BDS delivery approach are shown in Table 4. Fig. 8A shows the comparison between the experimental and simulation results of the MDS, and Fig. 8B shows the comparison between the experimental and

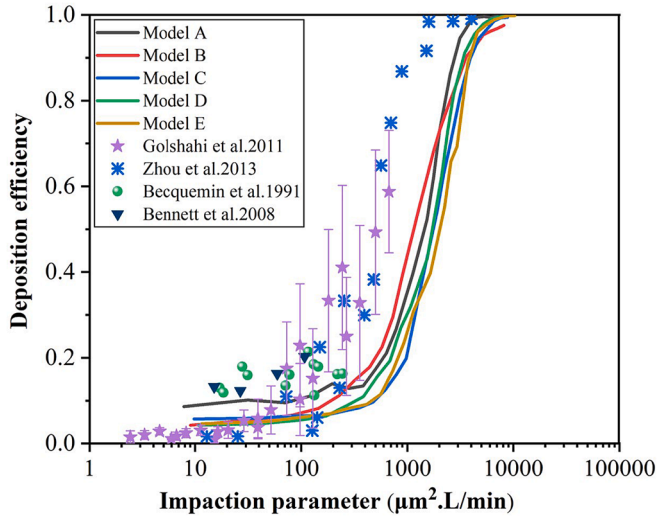

Fig. 7. Comparison of deposition results from this study with literature data. Deposition efficiency (DE) = the mass of drug deposited in a specific region / the total mass of drug released from the device × 100 %.

Table 4
Deposition results from in vitro experiments for MDS and BDS delivery approaches.

Regions	MDS		BDS	
	Resting inhalation (%)	High flow inhalation (%)	Resting inhalation (%)	High flow inhalation (%)
Vestibule	10.33	4.12	9.69	10.35
Turbinate	8.76	4.18	11.76	7.97
Septum	11.21	10.26	28.79	26.54
Olfactory	1.11	1.35	0.05	0.16
Maxillary sinus	2.53	1.97	0.65	0.07
Nasopharynx	5.21	6.11	3.15	2.01
Total	39.15	27.99	54.09	47.1

simulation results of the BDS. It can be observed that the experimental results are in good agreement with the simulation results. The above provides evidence that the present computational models are capable of producing reliable and accurate results.

3.2. Particle deposition patterns

3.2.1. Particle deposition pattern of MDS

All the results of this study are shown schematically by model D. The spatial deposition pattern using the MDS is shown in Fig. 9, and five particle sizes, 1 μm, 5 μm, 10 μm, 15 μm and 20 μm, were selected as representative particle sizes. Under low-flow inhalation conditions, an extensive deposition pattern was observed in the nasal cavity and nasopharynx, except in the vestibule. 1 μm particles were hardly trapped in the nasal cavity, suggesting that most inhaled particles escaped from the nose into the lower respiratory tract. The recovery of 15 μm and 20 μm particles was significantly higher in the nasal cavity, and were mainly deposited in the middle and inferior meatus. Under resting inhalation conditions, the captured particles, in general, were somewhat uniformly distributed in the nasal cavity and nasopharynx, and the deposition intensity was increased compared to low-flow inhalation conditions. Very few 1 μm particles were trapped in the nasal cavity, showing a relatively dispersed distribution pattern. Deposition of 15 μm and 20 μm particles was increased and concentrated, forming deposition spots in the nasal cavity, as illustrated in the black square in Fig. 9. Under high-flow inhalation conditions, the deposition distribution within the nasal cavity was significantly concentrated. The deposition intensity of 1 μm, 5 μm, and 10 um particles in the nasal cavity and nasopharynx was significantly higher compared to low-flow and resting inhalation conditions, with the formation of multiple isolated deposition spots. The deposition spots formed by 15 μm and 20 um particles were enlarged and significantly shifted anteriorly, mainly in the anterior 1/3 of the nasal cavity, and no significant deposition was seen in the nasopharynx. In all the cases, there were slight differences in the number of particles deposited between the right and left nasal chambers, and this is mainly attributed to the inter-chamber geometry difference.

3.2.2. Particle deposition pattern of BDS

The spatial deposition patterns of 1 μm, 5 μm, 10 μm, 15 μm and 20 μm particles using the BDS are shown in Fig. 10. Due to the unilateral property of the exhaled airflow, aerosol particles establish initial deposition in the left and right chambers sequentially. Under low-flow exhalation conditions, 1 μm and 5 μm particles showed a relatively dispersed distribution with low deposition intensity. The deposition of 15 μm particles increased and was mainly concentrated in the middle and inferior meatus of the LC, with a decrease in the RC. The 20 μm particles were mainly concentrated in the anterior part of the LC, with a significant reduction in deposition in the nasopharynx and RC. Under resting exhalation conditions, 1 μm particles were evenly distributed. Deposited 10 μm particles began to form deposition spots in the LC, with

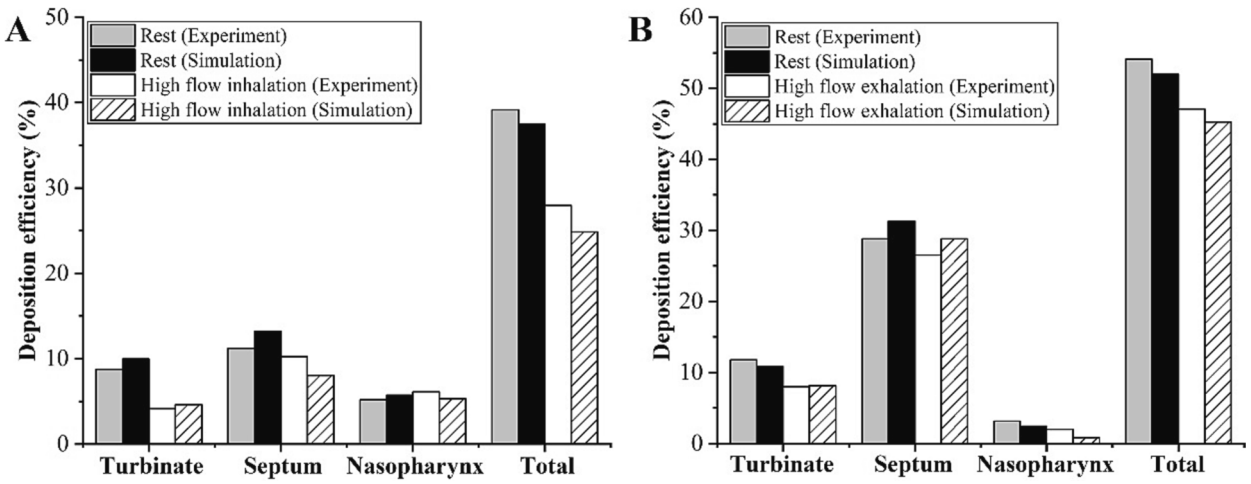

Fig. 8. Comparison of numerical simulation results and in vitro experimental results for the MDS (A) and BDS (B) delivery approach.

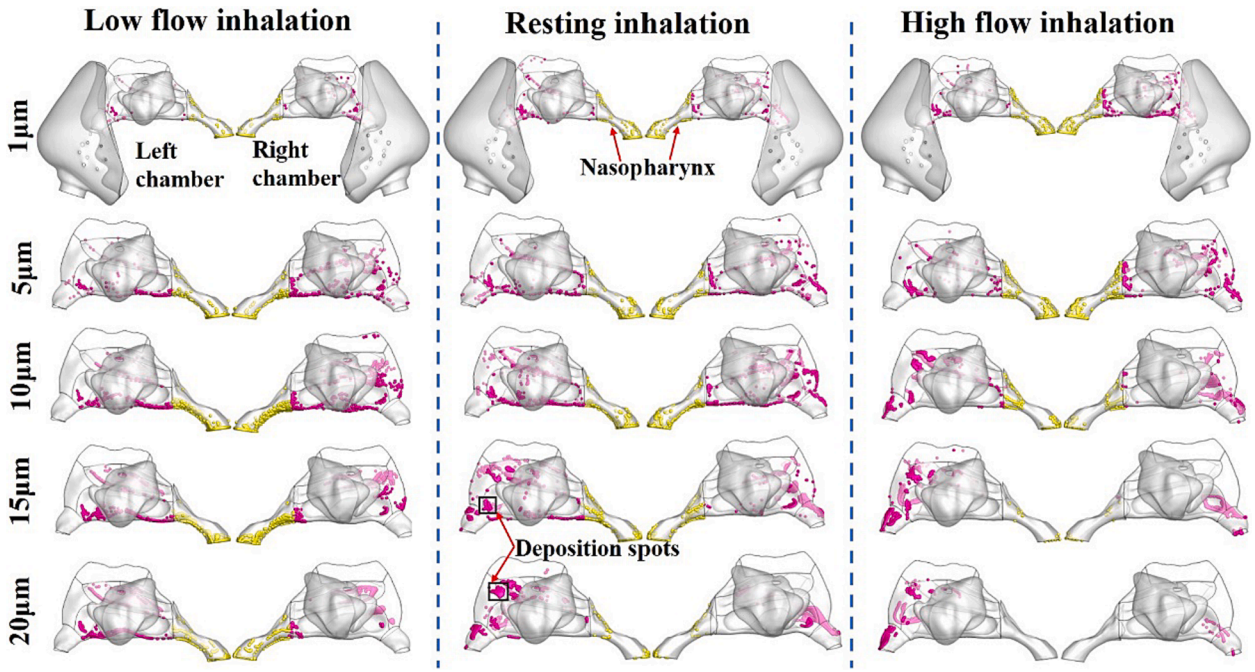

Fig. 9. Spatial deposition patterns of the MDS delivery approach at three inhalation flow rates. 1 μm, 5 μm, 10 μm, 15 μm and 20 μm were selected as representative particle sizes.

increased deposition in the nasopharynx and decreased deposition in the RC. Deposited 15 μm and 20 μm particles formed sheet-like aggregation in the anterior 2/3 of the LC, with significantly lesser deposition in the nasopharynx and RC. Under high-flow exhalation conditions, 1 μm and 5 μm particles were widely distributed and the deposition intensity was significantly higher than low-flow and resting exhalation conditions. 10 μm particles exhibited sheet-like aggregation in the anterior 2/3 of the LC, with a noticeable lower deposition in the nasopharynx and RC. The sheet-like aggregation formed by 15 μm and 20 μm particles was significantly shifted anteriorly, and no significant deposition was observed in the nasopharynx and RC.

3.3. Drug delivery efficiency analysis for the MDS

This section analyses the total and regional DEs for the MDS at low-flow, resting and high-flow inhalation conditions.

3.3.1. Analysis of the total DE for MDS

The total DE curve is shown in Fig. 11A. The total DE increased with the increase in particle size under low-flow inhalation conditions. The DE for 20 μm particles reached a peak (42.16 % ± 9.37 %), whereas for the low-inertia 1 μm particles, the DE was only 2.49 % ± 0.82 %. Under resting and high-flow inhalation conditions, the total DE exhibited an initial rise followed by a subsequent drop. The peak DEs were observed at 19 μm (Resting: 54.51 % ± 5.36 %) and 12 μm (High-flow: 43.18 % ± 13.28 %), respectively, while the lowest DEs were both found at 1 μm (Resting: 4.26 % ± 1.41 %; High-flow: 6.05 % ± 2.12 %). The studies by Shi et al. (2007) and Inthavong et al. (2009) have also shown that with an increase in particle diameter and flow rate, the deposition of inertial particles within the nasal cavity increased, and deposition hotspots notably shift anteriorly, primarily in the nasal valve area. Therefore, when the particle diameter and flow rate are sufficiently large, it may lead to the deposition of inertial particles before they even entered the nasal cavity, resulting in a decrease in DE within the nasal cavity. For the

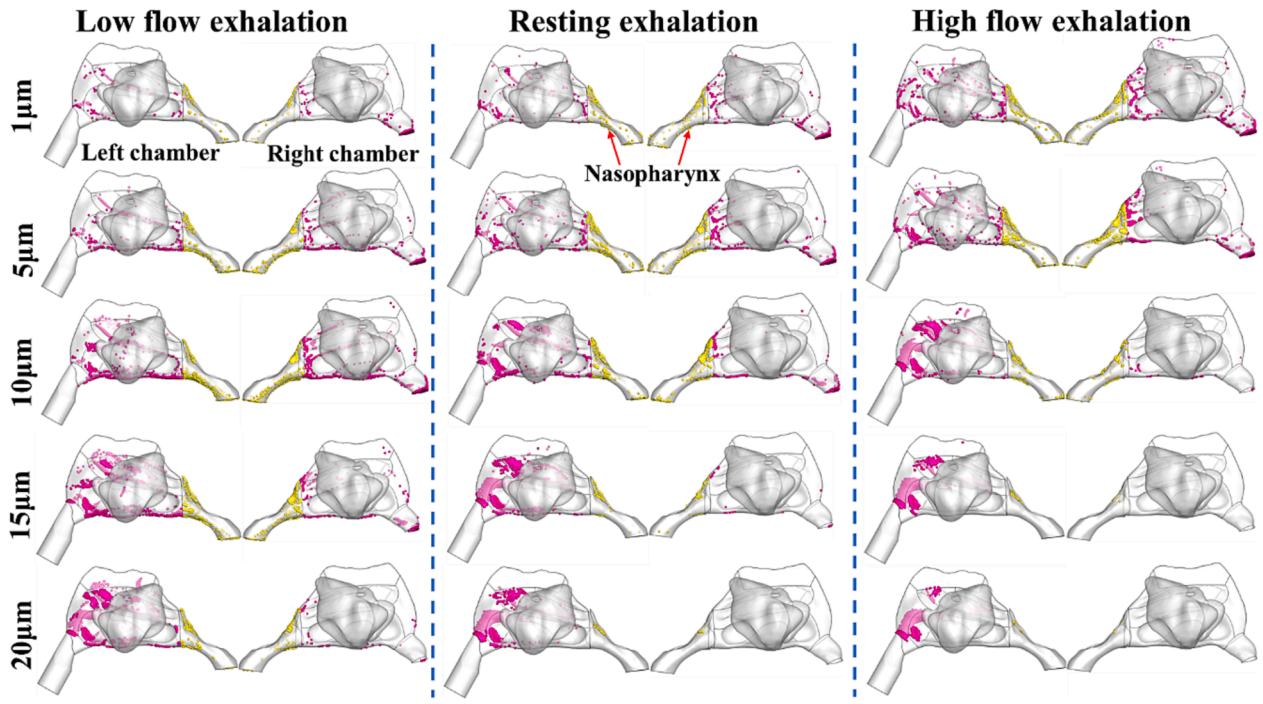

Fig. 10. Spatial deposition patterns of the BDS delivery approach at three exhalation flow rates. 1 μm, 5 μm, 10 μm, 15 μm and 20 μm were selected as representative particle sizes.

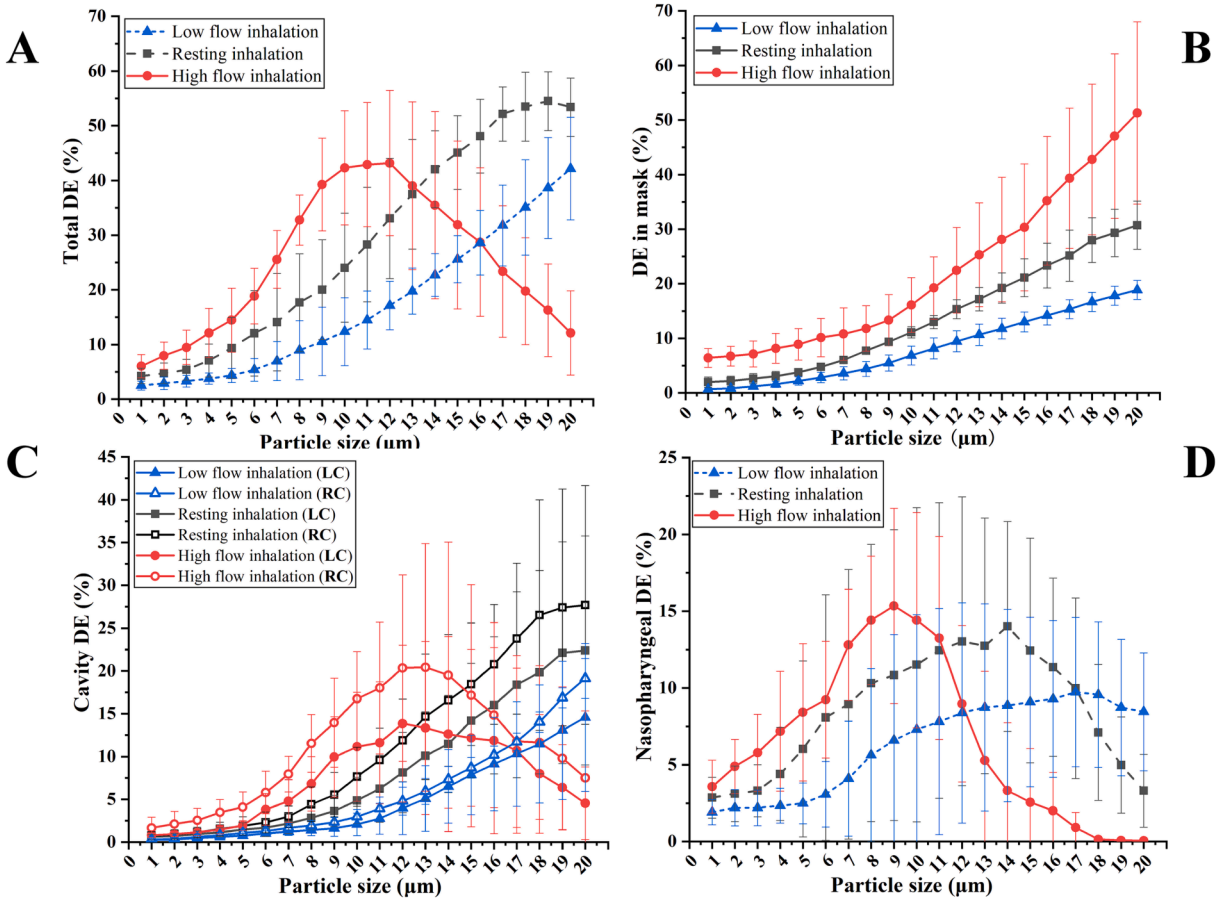

Fig. 11. Comparison of numerical simulation results for the MDS delivery approach at three inhalation flow rates: A: total DE, B: DE in the mask, C: chamber specific DE, and D: nasopharyngeal DE.

three inhalation flow rates, higher inhalation flow rate showed higher DEs when the particle diameter was less than 13 μm. For particles with diameters greater than 13 μm, the highest DE was observed during resting inhalation. For particles with diameters greater than 16 μm, the lowest DE was observed during high-flow inhalation. A higher inhalation flow rate led to greater deposition losses incurred by inertial particles passing through the mask (Fig. 11B).

3.3.2. Analysis of the chamber DE for MDS

Fig. 11C compares the DEs of the left and right chambers. Under low-flow and resting inhalation conditions, the DEs in the left and right chambers increased with increasing particle size, both reaching peaks at 20 μm (Low-flow: 14.58 % ± 8.63 % vs 19.13 % ± 2.33 %; Resting: 22.38 % ± 13.37 % vs 27.70 % ± 13.94 %). Under both of these inhalation conditions, higher inhalation flow rates showed higher DEs. Under high-flow inhalation conditions, the DEs in the left and right chambers exhibited an initial increase followed by a decrease, reaching peaks at 12 μm (13.85 % ± 9.16 %) and 13 μm (20.42 % ± 14.45 %), respectively. A common observation that applies to all three inhalation conditions was that the DE in the RC was higher than that in the LC, and this deposition difference was likely attributed to anatomical disparities between the chambers. Furthermore, the difference in peak DEs between the left and right chambers increased with higher inhalation flow rate (Low-flow: 4.55 %; Resting: 5.32 %; High-flow: 6.57 %).

3.3.3. Analysis of nasopharyngeal DE for MDS

The DE curve for the nasopharynx is shown in Fig. 11D. For all three inhalation conditions, the DE exhibited a trend of initial increase followed by a decrease, reaching peaks at 17 μm, 14 μm, and 9 μm, respectively (Low-flow: 9.74 % ± 4.85 %; Resting: 14.01 % ± 6.84 %; High-flow: 15.35 % ± 6.36 %). Under low-flow and resting inhalation conditions, the minimum DEs were observed at 1 μm (Low-flow: 1.92 % ± 0.82 %; Resting: 2.86 % ± 1.33 %). Under high-flow inhalation conditions, the minimum DE was nearly zero and occurred at 20 μm (0.06 % ± 0.07 %). When the particle diameter was less than 11 μm, higher inhalation flow rates showed higher DEs. Within the particle size range of 11–17 μm, the DE was at its highest during resting inhalation. For particles larger than 17 μm, higher inhalation flow rates showed lower DEs.

3.4. Drug delivery efficiency analysis for the BDS

This section analyses the total and regional DEs for the BDS under low-flow, resting and high-flow exhalation conditions.

3.4.1. Analysis of the total DE for BDS

The total DE curves are shown in Fig. 12A. Under three exhalation flow rates, the total DE curves all exhibited a trend of initially rapid increase followed by a slow decrease. The higher the exhalation flow rate, the DE peak tend to appear at small particles, and the DE decreased more rapidly after reaching the peak. Under three exhalation conditions, the total DE reached its peak at 17 μm (Low-flow: 95.11 % ± 0.72 %), 13 μm (Resting: 93.10 % ± 1.77 %), and 8 μm (High-flow: 90.23 % ± 2.08 %), respectively. Higher exhalation flow rates showed lower peak DEs. The lowest DEs were observed at 1 μm for three conditions (Low-flow: 4.23 % ± 2.22 %; Resting: 8.97 % ± 4.84 %; High-flow: 15.56 % ± 7.08 %). When the particle diameter was less than 9 μm, the higher the exhalation flow rate, the higher the DE. Within the particle size range of 9–14 μm, the DE was highest during resting exhalation. For particles larger than 14 μm, the higher the exhalation flow rate, the lower the DE. As the particle size increased, the deposition losses generated by inertial particles in the bi-directional device nosepiece gradually increased

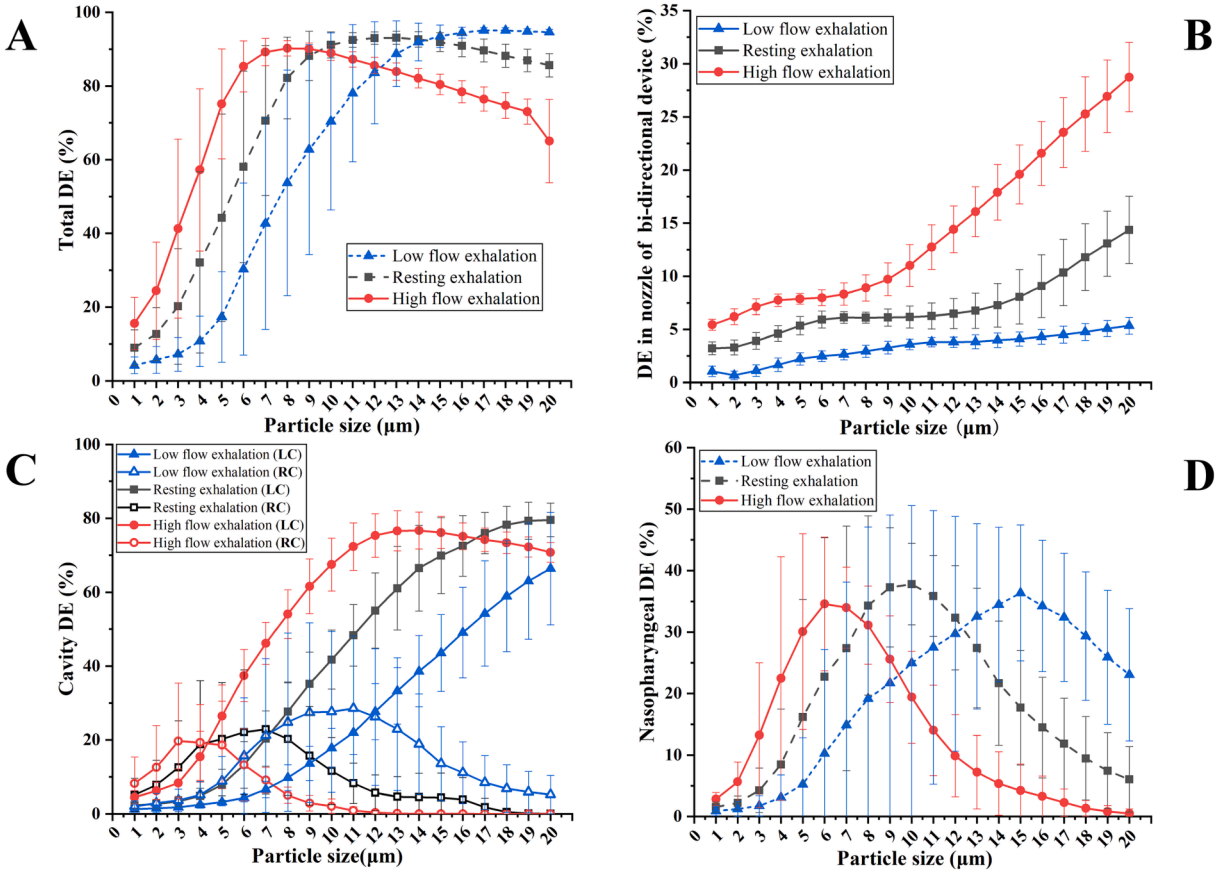

Fig. 12. Comparison of numerical simulation results for the BDS delivery approach at three exhalation flow rates: A: total DE, B: DE in the nosepiece, C: chamber specific DE, and D: nasopharyngeal DE.

(Fig. 12B). The higher the exhalation flow rate, the more pronounced the increase in deposition loss.

3.4.2. Analysis of the chamber DE for BDS

Fig. 12C compares the DEs between the LC and the RC. In this study, the bi-directional drug delivery device was connected to the left nostril; consequently, the majority of inhaled aerosols were initially captured by the LC, with only some residual particles passing through the nasopharynx into the RC. As a result, the DE in the LC was significantly higher than that in the RC. Under low-flow and resting exhalation conditions, the DE in the LC increased rapidly with increasing particle size, both reaching the peak at 20 μm (Low-flow: 66.36 % ± 15.24 %; Resting: 79.56 % ± 4.56 %). Under high-flow exhalation conditions, the DE in the LC first increased rapidly and then decreased slowly, reaching its peak at 14 μm (76.69 % ± 5.01 %). When the particle diameter was less than 17 μm, higher exhalation flow rates showed higher DEs in the LC. For particles larger than 17 μm, the DE in the LC was highest during resting exhalation. In comparison, the DE curves in the RC under the three exhalation conditions all exhibited a trend of initial increase followed by a decrease, remaining at low DE levels (less than 30 %). This is likely because most particles were deposited in the LC, resulting in few or no particles subsequently depositing in the RC. However, this deposition imbalance between the left and right chambers was significantly minimised for the low inertia particles, such as those with diameters that range between 1 and 4 μm. For 1–4 μm particles, it can be observed that the DEs in both the right and left chambers remain low at less than 20 %, and the RC has a slightly higher DE than the LC. One plausible explanation is that microparticles with smaller diameters have extremely low inertia, which makes them more susceptible to change direction following the main airflow, so that the majority of particles can follow the airflow into the RC and escape into the atmosphere through the right nostril. The study by Yarragudi et al. (2020) also demonstrated that microparticles with smaller diameters are more likely to reach the deeper nasal cavity and escape from the nasal passages, which provides some supporting evidence to the findings of this study.

3.4.3. Analysis of nasopharyngeal DE for BDS

The DE curve for the nasopharynx is shown in Fig. 12D. For all three exhalation conditions, the DE exhibited a trend of initial increase followed by decrease, forming three distinct deposition peaks. The higher the exhalation flow rate, the deposition peaks tend to appear at small particles, reaching peak DEs at 15 μm, 10 μm, and 6 μm, respectively (Low-flow: 36.36 % ± 11.06 %; Resting: 37.80 % ± 6.63 %; High-flow: 34.58 % ± 10.87 %). This is related to the deposition of large particles in the anterior part of the nasal cavity due to inertial impaction. In a numerical study of the nasal cavity in three healthy adult subjects conducted by Yarragudi et al. (2020), the deposition trend in the nasopharynx for the bi-directional delivery method was similar to ours but exhibited relatively lower DEs. This deposition difference is likely attributed to anatomical disparities between the adult and pediatric nasal cavities and differences in respiratory flow rates. Under low-flow and resting exhalation conditions, the DE at 1 μm was the lowest (Low-flow: 0.90 % ± 0.75 %; Resting: 1.54 % ± 0.82 %). Under high-flow exhalation conditions, the DE at 20 μm was close to zero (0.50 % ± 0.74 %). When the particle diameter was less than 7.5 μm, higher exhalation flow rates showed higher DEs. Within the particle size range of 7.5–12.5 μm, the DE was highest during resting exhalation. For particles larger than 12.5 μm, higher exhalation flow rates showed lower DEs.

3.5. Comparison of delivery efficiency of BDS and MDS

This section compares the total and regional DEs for the two delivery systems under low-flow, resting and high-flow inhalation and exhalation conditions.

3.5.1. Comparison of total DEs for MDS and BDS

The quantitative comparison of the total DEs for the two delivery systems is shown in Fig. 13. Overall, the BDS exhibited superior drug delivery performance for all particle sizes. Compared to the BDS, the MDS generated more deposition losses within the mask, significantly reducing the total DE in the nasal airway. Under low-flow and resting respiratory conditions, the difference in total DEs between the two delivery systems showed a trend of initially increasing and then decreasing. Under high-flow respiratory conditions, the deposition trends for both delivery systems were similar. For all three respiratory conditions, the smallest difference in total DEs was observed at 1 μm (Low-flow: 1.71 %; Resting: 4.71 %; High-flow: 9.51 %), and higher respiratory flow rates resulted in larger differences in total DEs. Under three respiratory conditions, the differences in total DEs between the two delivery systems were most pronounced at particle sizes of 14 μm, 9 μm, and 6 μm. In these cases, the BDS case consistently outperformed the MDS case, exhibiting DE enhancements of 69.23 % (Low-flow), 68.16 % (Resting), and 66.47 % (High-flow). Under three respiratory flow rates, the peak DEs for the BDS were approximately 1.71 to 2.26 times higher than those for the MDS (Low-flow: 95.11 % vs 42.16 %; Resting: 93.10 % vs 54.51 %; High-flow: 90.23 % vs 43.18 %), further confirming its superior drug delivery performance. However, the BDS showed greater inter-subject variability regarding DEs for most particle sizes.

3.5.2. Comparison of chamber DEs for MDS and BDS

The quantitative comparison of the chamber specific DEs for the two delivery systems is shown in Fig. 14. Given that LC is the chamber of interest, only the deposition results of the LC were compared for the BDS. Compared to the MDS, the BDS exhibited significantly higher chamber (target chamber) deposition for all particle sizes at three respiratory flow rates, greatly enhancing the delivery efficiency of drug aerosols. In a numerical study of adult nasal drug delivery conducted by Dong et al. (2017), the bi-directional delivery method similarly exhibited superior drug delivery performance, further corroborating our findings. At each respiratory flow rate, the chamber deposition trends for the two delivery systems were similar. Under all three respiratory conditions, the smallest DE difference was consistently observed at 1 μm. The higher the respiratory flow rate, the greater the difference in DE at 1 μm (Low-flow:1.00 %; Resting:1.55 %; High-flow: 2.83 %).

3.5.3. Comparison of nasopharyngeal DEs for MDS and BDS

As shown in Fig. 15, in comparison, the BDS exhibited better nasopharyngeal delivery performance, while the MDS showed overall nasopharyngeal DEs at a low level of below 16 %. An apparent reason is that the mask presents a larger surface area that traps particles before they can be entrained into the nasal airway. In addition, it is difficult for inertial particles to penetrate the nasal valve area to reach the nasopharynx deep in the nasal cavity when using the MDS. For low-inertia particles in the range of 1–3 μm, the BDS exhibited slightly lower DEs compared to the MDS, with the maximum DE difference being only 1.32 %. The higher the respiratory flow rate, the superior delivery performance of the BDS tends to cover all particle sizes.

3.5.4. Optimal particle size of MDS and BDS deposition peaks in the nasopharynx

The comparison of peak DEs in the nasopharynx for the two delivery systems is depicted in Fig. 16. Under three respiratory conditions, the BDS tended to be first to reach deposition peak at smaller particle sizes (15 μm vs 17 μm, 10 μm vs 14 μm, 6 μm vs 9 μm), and its peak DEs were substantially higher than those of the MDS (Low-flow: 36.36 % vs 9.74 %; Resting: 37.80 % vs 14.01 %; High-flow: 34.58 % vs 15.35 %). The BDS exhibited peak DEs in the nasopharynx that were 2.25 to 3.73 times higher than those of the MDS, providing strong evidence of its superior aerosol delivery performance. The higher the respiratory flow rate, the gap in peak DEs between the two delivery systems becomes smaller (Low-flow: 26.62 %; Resting: 23.79 %; High-flow: 19.23 %).

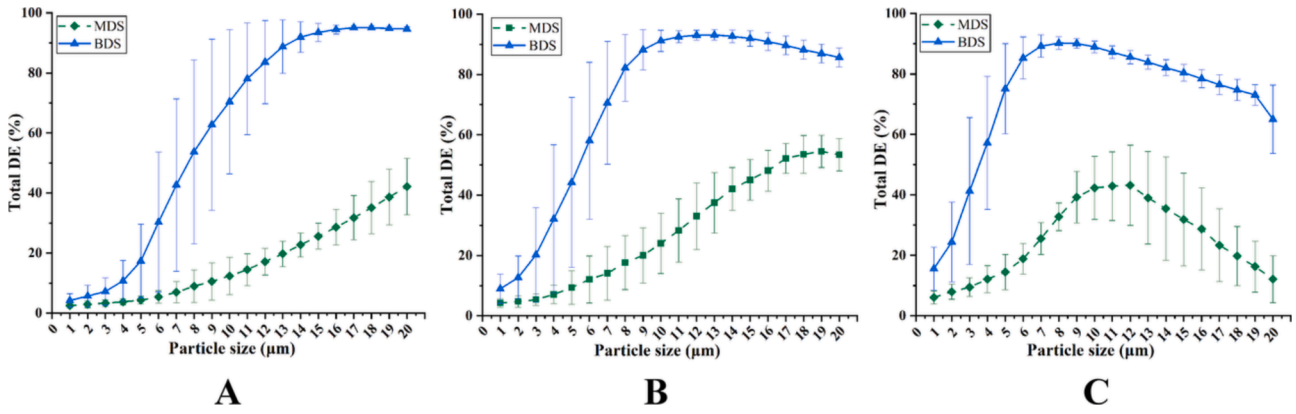

Fig. 13. Comparison of numerical simulation results for total DE between the MDS and the BDS delivery approach under low-flow (A), resting (B), and high-flow (C) respiratory conditions.

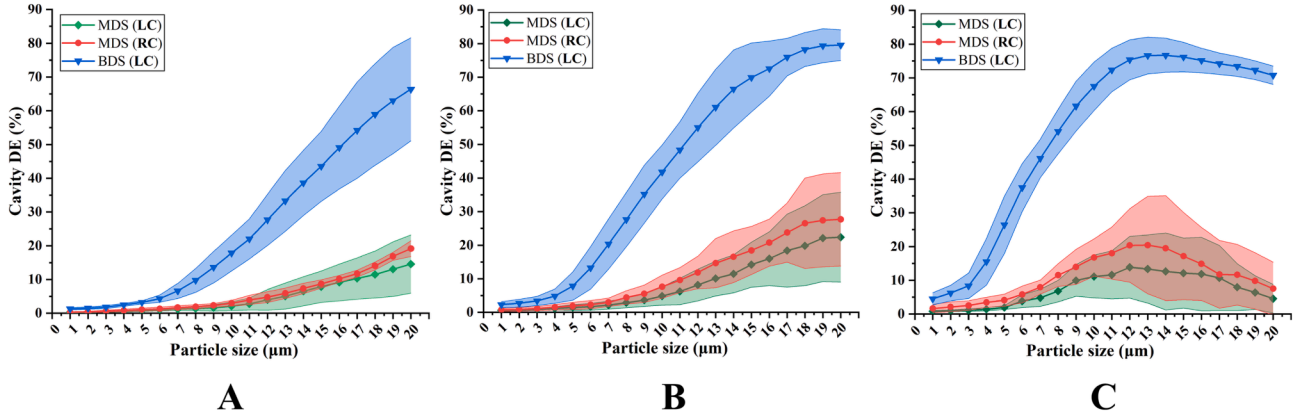

Fig. 14. Comparison of numerical simulation results for chamber specific DE between the MDS and the BDS delivery approach under low-flow (A), resting (B), and high-flow (C) respiratory conditions.

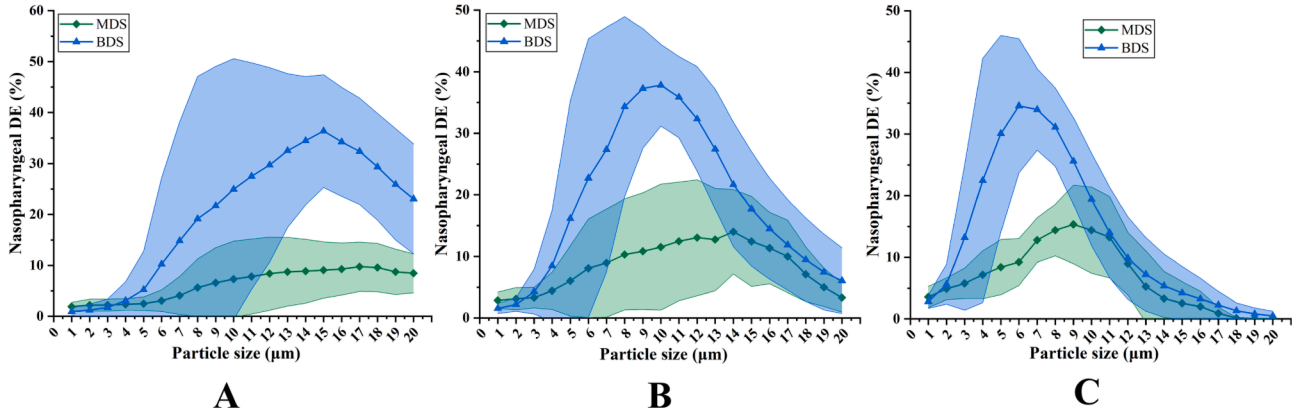

Fig. 15. Comparison of numerical simulation results for nasopharyngeal DE between the MDS and the BDS delivery approach under low-flow (A), resting (B), and high-flow (C) respiratory conditions.

Furthermore, the higher the respiratory flow rate, the deposition peaks tend to occur at smaller particle sizes; conversely, with lower respiratory flow rates, deposition peaks tend to occur at larger particle sizes. Therefore, for drug aerosols with different particle size distributions, drug delivery efficiency can be improved by adjusting the respiratory flow rate.

3.6. Effect of various AH on peak DEs in the nasopharynx

As shown in Fig. 17, the peak DE in the nasopharynx of children with severe AH was higher than that of those with moderate AH in all three respiratory conditions, in both MDS and BDS. This suggests that the greater the obstruction caused by adenoids in the nasopharyngeal airway, the more susceptible it is to the deposition of aerosol particles through impaction in the nasopharynx. For the disparity in nasopharyngeal deposition rates due to different degrees of AH, the disparity was

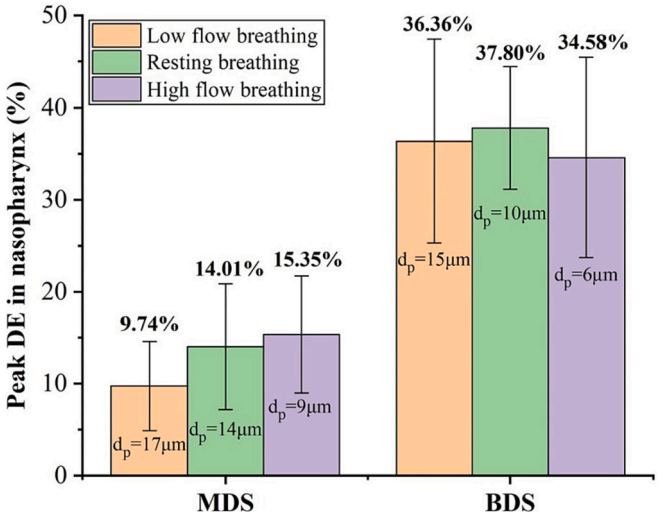

Fig. 16. Comparison of numerical simulation results for peak DEs in the nasopharynx between the MDS and the BDS delivery approach.

more pronounced for BDS than for MDS, which may be related to the different delivery principles of the two delivery systems. For children with moderate and severe AH, there were differences in the particle size corresponding to the peak deposition of MDS in the nasopharynx under the three respiratory conditions, suggesting that the changes in anatomical structure play a role in determining the optimal particle size. However, the peak deposition of BDS in the nasopharynx occurred at the same particle size across all considered respiratory conditions, with optimal particle size of 15 μm, 10 μm, and 6 μm for low-flow, resting and high-flow respiratory conditions, respectively. Both the high Peak DEs (~27 % - ~42 %) and consistent optimal particle sizes for moderate and severe AH provide BDS with a distinct advantage in treating children with varying degrees of AH. The peak DE results of MDS and BDS for subjects with varying levels of AH are anticipated to provide valuable insights for pharmaceutical industries in refining current inhalation devices. Additionally, current study offers practical guidance for physicians in selecting suitable devices when treating pediatric patients with AH.

This study is the first to compare the delivery efficiency of MDS and BDS in the nasopharynx of children with AH, which holds significant implications for improving aerosol therapy effectiveness in this distinct group. Similar to previous research findings (Dong et al., 2017; Shi et al., 2007; Schroeter et al., 2015; Kleven et al., 2005), we found that respiratory flow rate, particle size, and delivery method can significantly affect the transport and deposition of aerosol particles. For BDS and MDS, low-inertia particles in the range of 1–3 μm exhibited lower DEs in the nasal cavity and nasopharynx, with less inter-subject variability. In contrast, there was greater inter-subject variability in deposition in the nasal cavity and nasopharynx for larger inertial particles. The increase in respiratory flow rate and particle diameter did not increase the deposition dose in the nasopharynx. A plausible explanation is that the larger particles with higher inertia may have deviated from the main airflow and deposited in the anterior part of the nasal cavity by impaction. Overall, higher total and regional delivery efficiencies were obtained using BDS compared to MDS, but with relatively greater inter-subject variability at most particle sizes. These findings are significant for clinical applications as they offer insight into the depositional variability that may be encountered when using these two systems. This helps healthcare professionals better understand and plan treatment strategies to ensure that aerosol drug deposition within the patient's nasal cavity reaches the desired level.

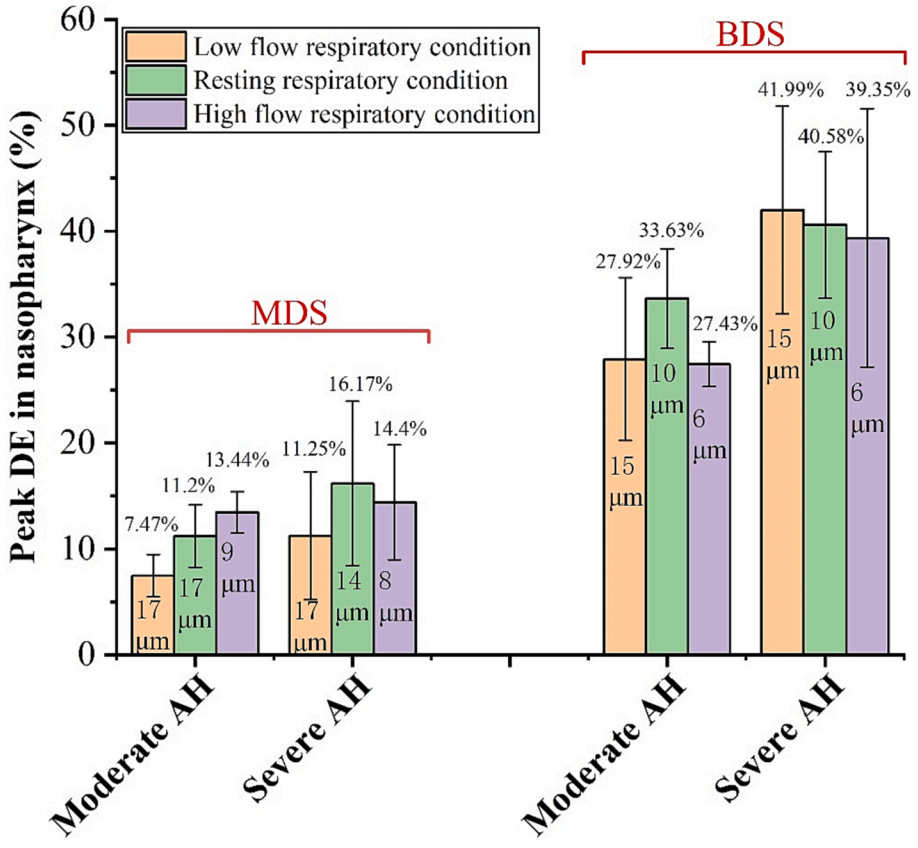

Fig. 17. Numerical simulation results of peak deposition in the nasopharynx of children with moderate AH versus severe AH.

4. Conclusion

This paper used an experimentally validated numerical model to investigate MDS and BDS's drug aerosol delivery performance. The two drug delivery methods' total and regional particle DEs were quantitatively compared. Compared to the MDS, the BDS can yield superior deposition in the nasal cavity and nasopharynx. For all three respiratory flow rates, the BDS consistently achieved higher nasopharyngeal deposition peaks at smaller particle sizes. The higher the respiratory flow rate, the deposition peaks tend to occur at smaller particle sizes; conversely, with lower respiratory flow rates, deposition peaks tend to occur at larger particle sizes. Therefore, drug delivery efficiency can be improved for aerosol drugs of different particle sizes by adjusting the respiratory flow rate. Furthermore, an optimal particle diameter exists for each respiratory flow rate, which maximises the drug delivery efficiency to the nasopharynx. The present study contributes to an in-depth understanding of air-particle flow characteristics under the interaction of the nasal drug delivery device with the pediatric nose. The findings of this study contribute to guiding early intervention in children with AH to enhance drug delivery efficiency, ultimately improving clinical treatment outcomes and effectively preventing the occurrence of complications.

CRediT authorship contribution statement

Zhenzhen Hu: Conceptualization, Data curation, Formal analysis, Methodology, Software, Validation, Writing – original draft. **Shaokoon Cheng:** Methodology, Writing – review & editing. **Siping Sun:** Formal analysis, Software. **Yusheng Wang:** Investigation, Software, Validation. **Miao Lou:** Validation, Visualization. **Ruiping Ma:** Formal analysis, Software. **Minjie Gong:** Software, Visualization. **Feilun Yang:** Validation, Visualization. **Guoxi Zheng:** Formal analysis, Funding acquisition, Supervision. **Ya Zhang:** Conceptualization, Formal analysis, Funding acquisition, Methodology, Writing – review & editing. **Jingliang Dong:** Conceptualization, Formal analysis, Funding acquisition, Methodology, Project administration, Supervision, Writing – review & editing.

Declaration of competing interest

The authors declare that they have no known competing financial interests or personal relationships that could have appeared to influence the work reported in this paper.

Data availability

Data will be made available on request.

Acknowledgements

This research was funded by the National Natural Science Foundation of China (grant number 82000960), the Key Research and Development Program of Shaanxi Province (grant number 2020GXLH-Y-017), the Science and Technology Planning Project of Yulin City (grant number CXY-2020-047), and the Australian Research Council (grant number DE210101549).

References

Adedeji, T.O., Amusa, Y.B., Aremu, A.A., 2016. Correlation between adenoidal nasopharyngeal ratio and symptoms of enlarged adenoids in children with adenoidal hypertrophy. Afr. J. Pediatr. Surg. 13, 14–19. https://doi.org/10.4103/0189-6725.181701.

Ahmad, Z., Kruger, K., Lautermann, J., Lippert, B., Tenenbaum, T., Tigges, M., Tisch, M., 2023. Adenoid hypertrophy-diagnosis and treatment: the new S2k guideline. HNO 71, 67–72. https://doi.org/10.1007/s00106-023-01299-6.

Bateman, N.D., Whymark, A.D., Clifton, N.J., Woolford, T.J., 2002. A study of intranasal distribution of azelastine hydrochloride aqueous nasal spray with different spray techniques. Clin. Otolaryngol. Allied. Sci. 27, 327–330. https://doi.org/10.1046/j.1365-2273.2002.00589.x.

Becquemin, M.H., Swift, D.L., Bouchikhi, A., Roy, M., Teillac, A., 1991. Particle deposition and resistance in the noses of adults and children. Eur. Respir. J. 4, 694–702.

Bennett, W.D., Zeman, K.L., Jarabek, A.M., 2008. Nasal contribution to breathing and fine particle deposition in children versus adults. J. Toxicol. Environ. Health A 71, 227–237. https://doi.org/10.1080/15287390701598200.

Cheng, Y.S., 2003. Aerosol deposition in the extrathoracic region. Aerosol Sci. Technol. 37, 659–671. https://doi.org/10.1080/02786820300906.

Chiang, C.E., Li, H.H., Rowley, D.D., Fang, T.P., Lin, H.L., 2023. Influence of aerosol mask design on fugitive aerosol concentrations during nebulization. Respir. Care 68, 10578. https://doi.org/10.4187/respcare.10578.

Djupesland, P.G., Skretting, A., Winderen, M., Holand, T., 2004. Bi-directional nasal delivery of aerosols can prevent lung deposition. J. Aerosol Med. 17, 249-259. https://doi. org/10.1089/jam. 2004.17.249.

Dong, J., Inthavong, K., Tu, J., 2016. Multiphase Flows in Biomedical Applications. In: Yeoh, G. (Ed.), Handbook of Multiphase Flow Science and Technology. Springer, Singapore. https://doi.org/10.1007/978-981-4585-86-6_16-1.

Dong, J., Shang, Y., Inthavong, K., Chan, H.K., Tu, J., 2017. Numerical comparison of nasal aerosol administration systems for efficient nose-to-brain drug delivery. Pharm. Res. 35, 5. https://doi.org/10.1007/s11095-017-2280-6.

Elwany, S., 1987. The adenoidal-nasopharyngeal ratio (AN ratio). Its validity in selecting children for adenoidectomy. J. Laryngol. Otol. 101, 569–573. https://doi.org/10.1017/s0022215100102269.

Farnoud, A., Baumann, I., Rashidi, M.M., Schmid, O., Gutheil, E., 2020. Simulation of patient-specific bi-directional pulsating nasal aerosol dispersion and deposition with clockwise 45° and 90° nosepieces. Comput. Biol. Med. 123, 103816 https://doi.org/10.1016/j.compbiomed. 2020.103816.

Farnoud, A., Tofighian, H., Baumann, I., Martin, A.R., Rashidi, M.M., Menden, M.P., Schmid, O., 2021. Pulsatile bi-directional aerosol flow affects aerosol delivery to the intranasal olfactory region: a patient-specific computational study. Front. Pharmacol. 12, 746420. https://doi.org/ 10.3389/fphar.2021.746420.

Fujioka, M., Young, L.W., Girdany, B.R., 1979. Radiographic evaluation of adenoidal size in children: adenoidal-nasopharyngeal ratio. AJR Am. J. Roentgenol. 133, 401-404. https://doi. org/10.2214 /ajr.133.3.401.

Golshahi, L., Noga, M.L., Thompson, R.B., Finlay, W.H., 2011. In vitro deposition measurement of inhaled micrometer-sized particles in extrathoracic airways of children and adolescents during nose breathing. J. Aerosol. Sci. 42, 474–488. https://doi.org/10.1016/j. jaerosci.2011.04.002.

Groneberg, D.A., Witt, C., Wagner, U., Chung, K.F., Fischer, A., 2003. Fundamentals of pulmonary drug delivery. Respir. Med. 97, 382–387. https://doi.org/10.1053/rmed.2002.1457.

Hofmann, W., 1982. Mathematical model for the postnatal growth of the human lung. Respir. Physiol. 49, 115–129. https://doi.org/10.1016/0034-5687(82)90106-2.

Hosseini, S., Golshahi, L., 2019. An in vitro evaluation of importance of airway anatomy in sub-regional nasal and paranasal drug delivery with nebulizers using three different anatomical nasal airway replicas of 2-, 5- and 50-Year-old human subjects. Int. J. Pharm. 563, 426–436. https://doi.org/10.1016/j.ijpharm.2019.04.019.

Hosseini, S., Wei, X., Wilkins, J.J., Fergusson, C.P., Mohammadi, R., Vorona, G., Golshahi, L., 2019. In vitro measurement of regional nasal drug delivery with flonase, ((R)) flonase((R)) sensimist, and MAD nasal in anatomically correct nasal airway replicas of pediatric and adult human subjects. J. Aerosol. Med. Pulm. Drug Deliv. 32, 374–385. https://doi.org/10.1089/jamp.2019.1523.

Hu, Z., Dong, J., Lou, M., Zhang, J., Ma, R., Wang, Y., Gong, M., Wang, B., Tong, Z., Ren, H., Zheng, G., Zhang, Y., 2023a. Effect of different degrees of adenoid hypertrophy on pediatric upper airway aerodynamics: a computational fluid dynamics study. Biomech. Model. Mechanobiol. 22, 1163–1175. https://doi.org/10.1007/s10237-023-01707-4.

Hu, Z., Ma, R., Wang, Y., Lou, M., Gong, M., Wang, B., Zheng, G., Dong, J., Zhang, Y., 2023b. Quantitative study of Artemisia pollens deposition in the upper airways of children with adenoidal hypertrophy. J. Aerosol. Sci. 172, 106191 https://doi.org/10.1016/j.jaerosci.2023. 106191.

Inthavong, K., Tu, J., Ahmadi, G., 2009. Computational modelling of gas-particle flows with different particle morphology in the human nasal cavity. J. Comput. Multiphase Flows 1, 57–82. https://doi.org/10.1260/175748209787387061.

Inthavong, K., Ge, Q., Se, C.M.K., Yang, W., Tu, J.Y., 2011. Simulation of sprayed particle deposition in a human nasal cavity including a nasal spray device. J. Aerosol. Sci. 42, 100–113. https://doi.org/10.1016/j.jaerosci.2010.11.008.

Inthavong, K., Tian, L., Tu, J., 2016. Lagrangian particle modelling of spherical nanoparticle dispersion and deposition in confined flows. J. Aerosol. Sci. 96, 56–68. https://doi.org/10.1016/j. jaerosci.2016.02.010.

Kesavan, J., Bascom, R., Laube, B., Swift, D.L., 2000. The relationship between particle deposition in the anterior nasal passage and nasal passage characteristics. J. Aerosol. Med. 13, 17–23. https://doi.org/10.1089/jam.2000.13.17.

Kimbell, J.S., Segal, R.A., Asgharian, B., Wong, B.A., Schroeter, J.D., Southall, J.P., Dickens, C.J., Brace, G., Miller, F.J., 2007. Characterization of deposition from nasal spray devices using a computational fluid dynamics model of the human nasal passages. J. Aerosol. Med. 20, 59–74. https://doi.org/10.1089/jam.2006.0531.

Kleven, M., Melaaen, M.C., Reimers, M., RØTNES, J.S., Aurdal, L., Djupesland, P.G., Sheldrake, C., 2005. The application of computational fluid dynamics (CFD) simulations for nasal drug delivery. In Fourth International Conference on CFD in the Oil and Gas, Metallurgical and Process Industries, SINTEF/NTNU Trondheim, Norway. 1-10.

Koca, C.F., Erdem, T., Bayindir, T., 2016. The effect of adenoid hypertrophy on maxillofacial development: an objective photographic analysis. J. Otolaryngol. Head Neck Surg. 45, 48. https://doi.org/10.1186/s40463-016-0161-3.

Li, L., Wilkins, J.J., Esmaeili, A.R., Rahman, N., Golshahi, L., 2023. In vitro comparison of local nasal vaccine delivery and correlation with device spray performance. Pharm. Res. 40, 537–550. https://doi.org/10.1007/s11095-022-03452-2.

Lin, H.L., Wan, G.H., Chen, Y.H., Fink, J.B., Liu, W.Q., Liu, K.Y., 2012. Influence of nebulizer type with different pediatric aerosol masks on drug deposition in a model of a spontaneously breathing small child. Resp. Care 57, 1894–1900. https://doi.org/10.4187/respcare.01652.

Lin, H.L., Harwood, R.J., Fink, J.B., Goodfellow, L.T., Ari, A., 2015. In vitro comparison of aerosol delivery using different face masks and flow rates with a high-flow humidity system. Respir. Care 60, 1215–1219. https://doi.org/10.4187/respcare.03595.

Niedzielski, A., Chmielik, L.P., Mielnik-Niedzielska, G., Kasprzyk, A., Boguslawska, J., 2023. Adenoid hypertrophy in children: a narrative review of pathogenesis and clinical relevance. BMJ Paediatr. Open 7, e001710. https://doi.org/10.1136/bmjpo-2022-001710.

Pawlowska-Seredynska, K., Umlawska, W., Resler, K., Morawska-Kochman, M., Pazdro-Zastawny, K., Krecicki, T., 2020. Craniofacial proportions in children with adenoid or adenotonsillar hypertrophy are related to disease duration and nasopharyngeal obstruction. Int. J. Pediatr. Otorhinolaryngol. 132, 109911 https://doi.org/10.1016/j.ijporl.2020.109911.

Schroeter, J.D., Tewksbury, E.W., Wong, B.A., Kimbell, J.S., 2015. Experimental measurements and computational predictions of regional particle deposition in a sectional nasal model. J. Aerosol. Med. Pulm. Drug Deliv. 28, 20–29. https://doi.org/10.1089/jamp.2013.1084.

Shi, H., Kleinstreuer, C., Zhang, Z., 2007. Modeling of inertial particle transport and deposition in human nasal cavities with wall roughness. J. Aerosol. Sci. 38, 398–419. https://doi.org/10.1016/j.jaerosci.2007.02.002.

Sun, Q., Dong, J., Zhang, Y., Tian, L., Tu, J., 2023. Numerical modelling of micron particle inhalation in a realistic nasal airway with pediatric adenoid hypertrophy: A virtual comparison between pre- and postoperative models. Front. Pediatr. 11, 1083699. https://doi.org/10.3389/fped.2023.1083699.

Thiriet, M., 2014. Biomathematical and Biomechanical Modeling of the Circulatory and Ventilatory Systems. Springer, New York.

Tong, X., Dong, J., Shang, Y., Inthavong, K., Tu, J., 2016. Effects of nasal drug delivery device and its orientation on sprayed particle deposition in a realistic human nasal cavity. Comput. Biol. Med. 77, 40–48. https://doi.org/10.1016/j.compbiomed.2016.08.002.

Wang, Y., Li, J., Leavey, A., O'Neil, C., Babcock, H.M., Biswas, P., 2017. Comparative study on the size distributions, respiratory deposition, and transport of particles generated from commonly used medical nebulizers. J. Aerosol Med. Pulm. Drug Deliv. 30, 132–140. https://doi.org/10.1089/jamp.2016.1340.

Wilkins, J.J., Golshahi, L., Rahman, N., Li, L., 2021. Evaluation of intranasal vaccine delivery using anatomical replicas of infant nasal airways. Pharm. Res. 38, 141–153. https://doi.org/10.1007/s11095-020-02976-9.

Xi, J., Wang, Z., Nevorski, D., White, T., Zhou, Y., 2017. Nasal and olfactory deposition with Normal and bidirectional intranasal delivery techniques: in vitro tests and numerical simulations. J. Aerosol. Med. Pulm. Drug Del. 30, 118–131. https://doi.org/10.1089/jamp.2016.1295.

Xi, J., Wang, Z., Si, X.A., Zhou, Y., 2018. Nasal dilation effects on olfactory deposition in unilateral and bi-directional deliveries: in vitro tests and numerical modeling. Eur. J. Pharm. Sci. 118, 113–123. https://doi.org/10.1016/j.ejps.2018.03.027.

Yarragudi, S.B., Kumar, H., Jain, R., Tawhai, M., Rizwan, S., 2020. Olfactory targeting of microparticles through inhalation and bi-directional airflow: effect of particle size and nasal anatomy. J. Aerosol. Med. Pulm. Drug Deliv. 33, 258–270. https://doi.org/10.1089/jamp. 2019.1549.

Zhou, Y., Xi, J., Simpson, J., Irshad, H., Cheng, Y.S., 2013. Aerosol deposition in a naso-pharyngolaryngeal replica of a 5-year-old child. Aerosol. Sci. Technol. 47, 275–282. https://doi.org/10.1080/02786826.2012.749341.

Zwierz, A., Masna, K., Domagalski, K., Burduk, P., 2023. 150th Anniversary of global adenoid investigations: unanswered questions and unsolved problems. Front. Pediatr. 11, 1179218. https://doi.org/10.3389/fped.2023.1179218.